Corrosion Science 51 (2009) 677–682

Contents lists available at ScienceDirect

Corrosion Science

journal homepage: www.elsevier.com/locate/corsci

# The influence of crystallographic orientation distribution on 316LVM stainless steel pitting behavior

Arash Shahryari [a,*], Jerzy A. Szpunar [b], Sasha Omanovic [a]

[a] Department of Chemical Engineering, McGill University, 3610 University Street, Montreal, Que., Canada H3A 2B2
[b] Department of Mining and Materials Engineering, McGill University, Montreal, Que., Canada H3A 2B2

ARTICLE INFO

*Article history:*
Received 18 November 2008
Accepted 17 December 2008
Available online 27 December 2008

*Keywords:*
A. Stainless steel
C. Pitting corrosion
Texture
Crystallographic orientation
Prediction

ABSTRACT

In this research, the influence of crystallographic orientation on pitting corrosion susceptibility of 316LVM stainless steel surface has been investigated using orientation imaging microscopy (OIM) technique. It has been shown that the susceptibility of the surface to pitting corrosion depends strongly on the crystallographic orientation of the planes parallel to the surface. This has revealed an anisotropic nature of pitting initiation on the surface, suggesting that controlling the texture of the material can be considered as a means of ameliorating the material's pitting resistance. The generalized spherical harmonic functions have been used to express the pitting susceptibility of various crystallographic planes. Using the proposed formula and the texture inverse pole figure of the investigated material (obtained from orientation distribution function, ODF), the pitting susceptibility index (PSI) of the surface is predicted based on texture measurements. The results obtained thus demonstrate a novel method of improving pitting resistance of SS316LVM by designing the desired texture.



## 1. Introduction

Susceptibility of the surface to pitting corrosion defines one of the major problems pertaining the selection of stainless steels (SSs) in a variety of applications. For instance, SSs are widely used in biomedical applications and therefore, the selection of these materials for the design of various biomedical implants is directly dictated by the level of pitting resistance they offer in physiological environments [1,2]. Austenitic stainless steels such as SS316L, where "L" stands for a low content of carbon, have been extensively used in biomedical applications. However, one of the problems associated with SS316L is the presence of relatively high content of sulfur, resulting in formation of MnS inclusions, which are pitting-susceptible sites [3,4]. Therefore, a nobler and more expensive version of SS316L, known as SS316LVM (where "VM" stands for "Vacuum Melted") offers lower susceptibility to pitting, and is thus a more commonly used type of SSs for orthopaedic applications [5].

Pitting corrosion, initiated on the surface of the material, can adversely affect both its biocompatibility, when used in a human body due to the uncontrolled ion release [6,7], and also its mechanical integrity due to the created stress concentrated spots on the surface. In fact, pitting corrosion is categorized as one of the most destructive types of localized corrosion on SSs which can influence their suitability and durability for a verity of applications. Therefore, numerous efforts have been made to understand the mechanism and nature of pitting corrosion, on one hand, and the key factors controlling its occurrence, on the other hand [4,8–11].

Metallurgical variables have been shown to influence the corrosion resistance of austenitic SSs [12]. The effect of alloying elements on the material's pitting resistance has also been widely reported in literature [13–16]. The texture of austenitic SSs is a parameter which has been shown to have an effect on the material's surface pitting resistance [17,18]. Mechanical deformation or annealing of the material is known to influence the orientation of the grains and the material's texture. Investigating the effect of rolling and heat treatment, Phadnis et al. [19] showed that the cold rolled SS304 surface exhibits a significantly better corrosion resistance than the heat treated surface. The superior corrosion behavior of the rolled material was attributed to the higher content of Cr in the oxide passive film of the rolled SS surface. On contrary, Abreu et al. [20] have claimed that increasing the cold deformation of SS316L, results in an increase in the surface pit density. The lower pitting resistance of the deformed material has been related to the defects created during deformation, which in turn act as pitting nucleation sites. A decrease in the corrosion resistance of SS301 as a result of deformation has also been reported by Barbucci et al. [21]. The effect of texture and surface morphology on the corrosion behavior of metallic coatings has also been investigated and cited in literature [16,18].

* Corresponding author. Tel.: +1 514 562 5055; fax: +1 514 398 6678.
*E-mail address:* arash.shahryari@mail.mcgill.ca (A. Shahryari).

0010-938X/$ - see front matter © 2008 Elsevier Ltd. All rights reserved.
doi:10.1016/j.corsci.2008.12.019

The influence of austenitic SS texture on its surface pitting resistance in chloride containing solutions has been investigated and reported in literature [17,19,22]. The variation of pitting potential with respect to the thickness-reduction percentage induced by cold rolling of SS has been studied and it has been shown that the surface pitting susceptibility is dependent on the percentage of cold rolling thickness reduction.

Considering the existing anisotropic nature of corrosion behavior of austenitic SSs, it would be of a critical importance to establish the correlation between pitting corrosion resistance and the type of crystallographic plane. That would make it possible to develop a model which determines the pitting susceptibility of materials having different texture, and could eventually lead to a novel method of improving the pitting resistance through texture control. Novel thermomechanical processing that allows manufacturing the texture that improves the surface pitting resistance of the material for different working environments can be developed.

In the present work, an effort has been made to study the variation of SS316LVM pitting resistance with crystallographic orientation of grains determined using orientation imaging microscopy (OIM) technique. The obtained results have been used to develop a mathematical formula that illustrates the correlation between texture and the pitting resistance of austenitic SS316LVM.

## 2. Experimental details

Stainless steel 316LVM samples of dimensions 2 cm × 2 cm × 1 cm were used in the experiments reported here. Chemical composition of SS316LVM is shown in Table 1. Prior to each experiment, the sample surface was wet-polished successively starting from 600 up to 4000-gradation abrasive sandpaper, followed by sonication in deionized water for 5 min. The samples were further polished using an emulsion of 0.05 μm SiC particles under high-frequency vibration conditions, to obtain a mirror-like surface. Then, the samples were cleaned using a smooth polishing cloth and deionized water to ensure the removal of the polishing emulsion particles. This was followed by sonication of samples in deionized water to remove any polishing residues and finally by degreasing the surface in ethanol.

Pitting corrosion was induced on the surface using potentiodynamic polarization of the surface. The electrochemical experiments were carried out in a single-compartment electrochemical cell. The counter electrode (CE) was a platinum wire, and a saturated calomel electrode (SCE) was used as the reference electrode (RE). A SS316LVM sample was the working electrode (WE).

The pitting polarization was performed in oxygen-free 1 M NaCl aqueous solution, by continuously purging the electrolyte with argon, starting 30 min prior to, and continuing during the measurements. Once the working electrode was placed inside the electrolyte, the sample surface was stabilized at open-circuit potential (OCP) in the solution for a period of one hour. Then, linear polarization was performed starting from 50 mV negative of OCP toward a more positive potential at which a current density of 0.1 mA $cm^{-2}$ was reached.

An Autolab potentiostat/galvanostat/frequency_response_analyzer (Ecochemie), PGSTAT30/FRA2, controlled by the GPES/FRA v.4.9.5 software was used in electrochemical/corrosion experiments. Texture measurements were carried out by scanning electron microscopy (SEM) using a Philips XL30 FEG (field emission gun) SEM equipped with a TSL orientation imaging microscopy (OIM) camera. The operation accelerating voltage was 30 kV and the working distance was kept at 10 mm.

**Table 1**
Chemical composition of AISI 316LVM stainless steel (wt.%).

| Fe | Cr | Ni | C | Mo | Mn | S | Si |
|---|---|---|---|---|---|---|---|
| bal | 16.57 | 10.34 | 0.016 | 2.13 | 1.54 | 0.001 | 0.54 |

| P | Cu | Sn | Co | N | O | Nb |
|---|---|---|---|---|---|---|
| 0.024 | 0.28 | 0.009 | 0.09 | 0.03 | 34 ppm | 0.01 |

## 3. Results and discussions

### 3.1. Crystallographic orientations

Fig. 1 shows an orientation imaging microscopy (OIM) map of the surface of SS316LVM, obtained by electron back-scatter diffraction (EBSD). The map shows the distribution of different grain orientations on the 316LVM surface. It is seen, from the color code of different crystal planes, that grains are rather randomly distributed, indicating that the texture is weak. Such weak texture was especially important for this work since it allowed observing the differences in pitting behavior of the differently oriented grains. A large number of twin-type grain boundaries are observed on the OIM map, which indicates the contribution of twinning to deformation mechanism in stainless steel.

In order to investigate the correlation between the pitting corrosion and the surface texture, the sample was polarized in saline solution after stabilization at OCP. Fig. 2 shows the potentiodynamic polarization curve of the SS316LVM surface recorded in 1 M NaCl solution. Generally, the polarization of stainless steel in

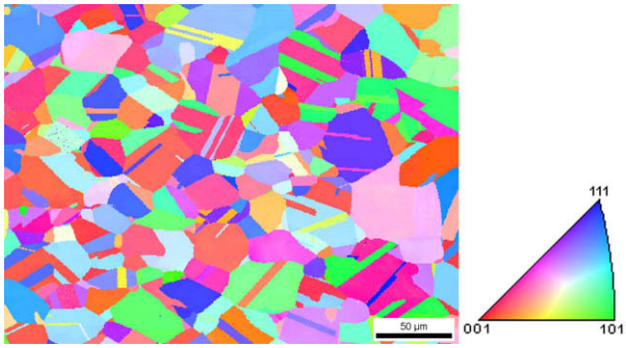


**Fig. 1.** Inverse pole figure map of an area on the surface of 316LVM sample. The image shows the EBSD data obtained by TSL orientation imaging microscopy (OIM) technique.

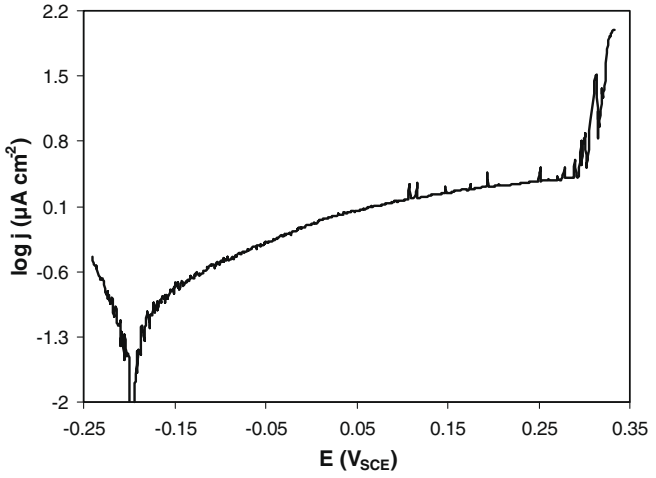


**Fig. 2.** Pitting polarization curve of the SS316LVM surface recorded at 22 °C in 1 M NaCl solution. Scan rate = 1 mV $s^{-1}$.

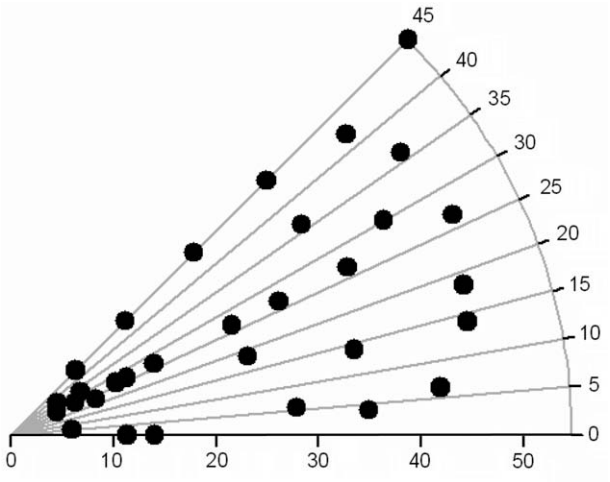


**Fig. 3.** Distribution of the crystallographic orientations on SS316LVM surface for the corrosion measurements. The coordinates in the figure are the spherical polar coordinates ($0° \leqslant \Phi \leqslant 53°$, the abscissa and $0° \leqslant \beta \leqslant 45°$, the polar angle) in the inverse pole figure representation. Different areas of the surface were randomly mapped and the grains included in the selected area were investigated.

a metastable pitting potential region (between the OCP and pitting potential) results in the formation of metastable pits on the surface, followed by their repassivation, which is manifested as a series of sharp current transients (spikes) [23]. In fact, only a fraction of the initiated metastable pits can grow and form stable pits, while the rest of pits repassivate and do not propagate. Nevertheless, as the number of metastable pits on the surface increases, the probability of the stable pits formation also increases. Accordingly, the occurrence of current spikes on the anodic branch of the polarization curve (Fig. 2) at potentials higher than 0.08 V indicates the initiation of metastable pitting on the surface. In the microscopic scale, these spots would leave micro-pits on the surface, the frequency of which is usually interpreted as a direct measure of the surface susceptibility toward pitting corrosion.

Since this material shows relatively weak texture, the occurrence of different crystal planes in the selected maps was expected to be random. Fig. 3 shows the inverse pole figure representation of the crystallographic planes distribution in the direction perpendicular to the investigated surface of the specimen. The possibility of observing and counting pits on a variety of crystallographic planes is necessary in order to establish a mathematical correlation between the orientation of grains and the pitting behavior of stainless steel specimens.

In order to be able to observe the frequency of occurrence of pits on the surface, the number of pits on different crystallographic planes was to be determined. Fig. 4a shows a typical OIM map of a randomly selected area on the SS316LVM surface after a pitting polarization experiment in saline solution. The included color code inverse pole figure map in Fig. 4 indicates the crystallographic orientation of different grains shown in Fig. 4a. The distribution of the micro-pits on the same grains is shown in Fig. 4b. The presence of micro-pits on the various crystallographic planes exposed to pitting is quite evident in Fig. 4b. The pits density on grains of different orientations was calculated using image analysis techniques and was used as a measure of the susceptibility of grains to pitting corrosion. The significant difference between the pit densities for different crystallographic planes indicates that the pitting resistance is a strongly anisotropic property in the austenitic stainless steels. On other hand, it is well known that pitting corrosion on stainless steels is generally triggered at susceptible surface spots, such as MnS inclusions on SS316L [3,15,24]. Our investigations have shown that MnS inclusions are not present in this type of stainless steel, 316LVM. This further supports the fact that the difference in the surface pitting susceptibility on different grains observed in Fig. 4, originates from the type of the grains' crystallographic orientation rather than the chemical composition of the material.

Using a similar approach, the values of the pit densities for all the orientations presented in Fig. 3 were determined by measuring the number of observed pits on an arbitrary unit surface area. In order to be able to relatively determine the pitting susceptibility of the surface to pitting corrosion, the pit-density values were then normalized so that these values yield a dimensionless pitting susceptibility index (PSI) in the range of $0 \leqslant \mathrm{PSI} \leqslant 1$ (all the values were divided by the maximum pit density obtained). The distribution of the PSI values is shown on the inverse pole figure repre-

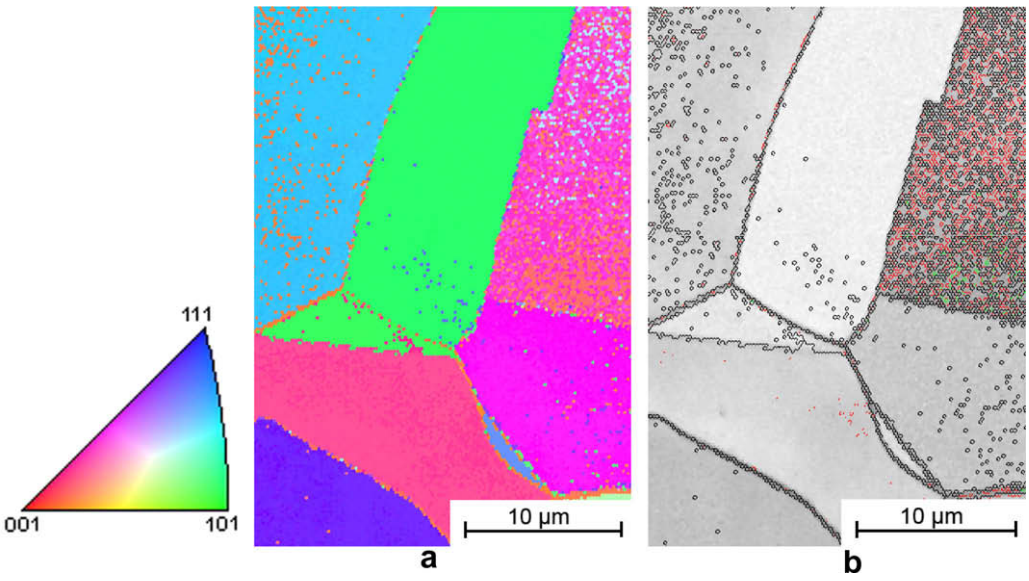


**Fig. 4.** A typical OIM map of an area on the surface of SS316LVM sample. (a) Crystallographic orientation of the gains marked by color and (b) the distribution of micro-pits on the grains shown in (a). The EBSD images were obtained by TSL orientation imaging microscopy (OIM) technique. (For interpretation of the references to colour in this figure legend, the reader is referred to the web version of this article.)

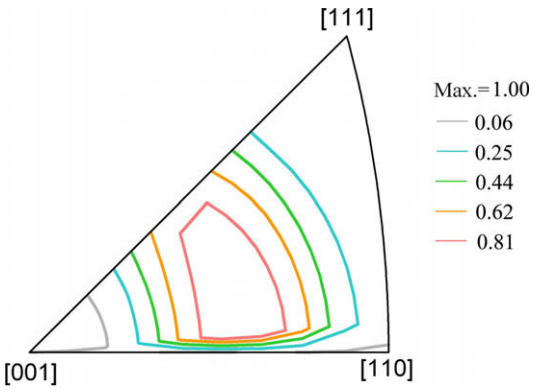


**Fig. 5.** 2-D Representation of the relative surface pitting susceptibility index (PSI) for various crystallographic planes. The coordinates in the figure are the spherical polar coordinates ($0° \leqslant \Phi \leqslant 53°$, the abscissa and $0° \leqslant \beta \leqslant 45°$, the polar angle) in the inverse pole figure representation.

sented in Fig. 5. The values presented in Fig. 5 are just an indication of the relative susceptibility of various crystallographic orientations to pitting corrosion (defined as PSI) and therefore do not represent the actual density of pits on the surface. The results presented in Fig. 5 indicate that the planar orientation {111} and {100} have the lowest susceptibility to pitting corrosion. These planes are associated with the orientations with high atomic density. The anisotropic nature of pitting on the pure iron in distilled water has been also shown by Kruger [25]. The pitting behavior of {111}, {110} and {100} planes cut out of a single crystal was investigated and it was concluded that the number of pits on these three planes decreases significantly at this order: {110} > {100} > {111}, which is in agreement with the trend observed in this work. Taking into account the planar atomic density of these three planes in FCC system, with {111} having the highest atomic density, it is logical to conclude that the observed trend in the pitting susceptibility of crystallographic orientations, is related to the atomic density of each plane. The dependence of the pitting kinetics and morphology on the planar atomic density has been previously reported [26–28]. However, in order to more clearly elucidate the main origin of the observed trend, fundamental analysis and molecular dynamic simulation of the atoms in various crystallographic orientations has to be further investigated.

### 3.2. Modeling the orientation-pitting data

As it was mentioned earlier, the pit susceptibility index (PSI) values measured on different crystallographic planes, were plotted in the inverse pole figure that represents the pitting susceptibility as a function of the spherical polar coordinates, $\beta$ and $\Phi$, that describe the orientation of crystallographic plane ($hkl$) in the crystallographic reference frame (Fig. 5). This frame is defined by three directions of <100> type. The crystallographic symmetry of FCC structure allows for representing all crystallographic planes in the space defined by $\beta$ ($0° \leqslant \beta \leqslant 45°$) and $\Phi$ ($0° \leqslant \Phi \leqslant 53°$). The inverse pole figure, used to represent the PSI, describes therefore the frequency of the pits observed at different crystallographic planes on the specimen surface. To represent the pit frequency (PSI) changes, $PSI_{y_i}(h)$ function is used. It expresses the PSI as a function of the orientation ($\beta$,$\Phi$) of vector $h$, which represent directions normal to the various crystallographic planes. This function can be represented as series of generalized spherical harmonics:

$$PSI_{y_i}(h) = \sum_{l=0}^{\infty} \sum_{m=1}^{M(l)} A_l^m k_l^m(h) \tag{1}$$

where, $A_l^m$ is series of constants for various values of $l$. The spherical harmonic functions $k_l^m(h)$ in Eq. (1) is defined by the following equation:

$$k_l^m(\Phi, \beta) = \frac{1}{\sqrt{2\pi}} e^{im\beta} \overline{P}_l^m(\Phi) \tag{2}$$

where the generalized Legendre functions $\overline{P}_l^m(\Phi)$ are defined as:

$$\overline{P}_l^m(\Phi) = \sum_{s=-l}^{+l} a_l^{ms} e^{is\Phi} \tag{3}$$

Eq. (3) can be further simplified:

$$\overline{P}_l^m(\Phi) = \sum_{s=0}^{l} a_l^{ms} \cos s\Phi \quad (\text{for } m - \text{even}) \tag{4}$$

$$\overline{P}_l^m(\Phi) = \sum_{s=1}^{l} a_l^{ms} \sin s\Phi \quad (\text{for } m - \text{odd}) \tag{5}$$

Due to the specific symmetry of the crystal and the specimen reference frame,

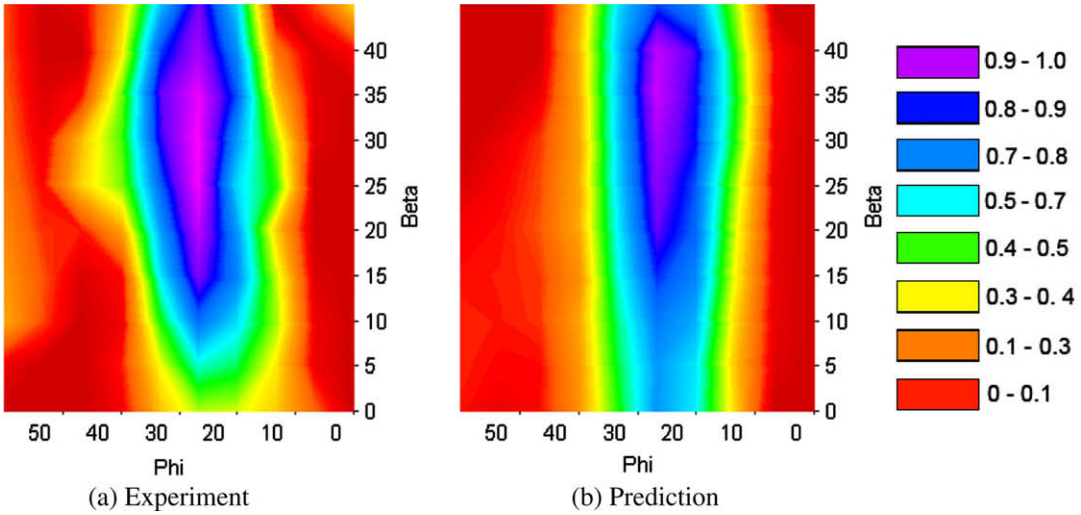


**Fig. 6.** 2-D Representation of the relative surface pitting susceptibility index (PSI) for various crystallographic orientations: (a) the experimental data and (b) the predicted values using the developed model. The coordinates in the figure are the spherical polar coordinates ($0° \leqslant \Phi \leqslant 53°$, the abscissa and $0° \leqslant \beta \leqslant 45°$, the polar angle) in the inverse pole figure representation.

$$a_l^{ms} = 0 \qquad (\text{for } l + s \text{ odd}) \tag{6}$$

The coefficients $a_l^{ms}$ can be found in literature [29].

The number of linearly independent spherical harmonics up to $l = 10$ for the cubic system was used. The values $l$, $M(l)$ were chosen to be 10 and 1, respectively. Eq. (1) was fitted to experimental PSI data, using the least-square-fitting method in Matlab software in order to find the values of the constants $A_l^m$ in Eq. (1).

Using the obtained constants in Eq. (1), the values of the pit densities were predicted over a range of $\beta$ and $\Phi$ which is sufficient for representing crystallographic planes of different types due to crystallographic symmetry of FCC in the interval of crystallographic orientations defined by $\beta$ ($0° \leqslant \beta \leqslant 45°$) and $\Phi$ ($0° \leqslant \Phi \leqslant 53°$). This would result in $10 \times 12$ points with a 5° interval representing the entire angular range of the inverse pole figure. Fig. 6a presents the PSI values of various crystallographic orientations obtained from the experimental data, while Fig. 6b shows the predicted PSI values obtained from the developed model using Eq. (1) and the constants in Table 2. A rectangular representation of the data has been used in order to clearly compare the experimental and predicted PSI distributions. Although there is a slight deviation in the predicted values relative to the experimental data at low values of $\beta$, there is a general agreement between the PSI values obtained from predicted and experimental values. Particularly, the agreement between the predicted and experimental data is evident for the main crystallographic orientations, {111}, {110} and {100}. In order to be able to apply the proposed model to a recorded texture measurement, the mean PSI is to be evaluated. Fig. 7a shows the orientation distribution function (ODF) and the normal direction inverse pole figure (Fig. 7b) of a 316LVM substrate obtained by XRD data and calculated using TexTools software. Since the pitting polarization experiments are normally conducted on the sample surface, only the orientation of the crystallographic planes exposed to the surface of the sample is thus important. Therefore, the inverse pole figure shown in Fig. 7b is related to the normal direction of the sample. The mean value of pitting susceptibility index, $\overline{PSI}$, can be defined for a SS316LVM substrate using the following equation:

$$\overline{PSI} = \frac{\oint \int PSI(\beta,\Phi) \cdot I(\beta,\Phi) \sin(\beta) d\beta \cdot d\Phi}{\oint \int I(\beta,\Phi) \sin(\beta) d\beta \cdot d\Phi} \tag{7}$$

$PSI$ ($\beta$, $\Phi$) is the pitting susceptibility index for an orientation specified by $\beta$ and $\Phi$ and $I(\beta, \Phi)$ is the calculated intensity value of the inverse pole figure for the direction normal to the specimen. The ODF presented in Fig. 7a evidences the presence of a cube texture for the studied substrate. Calculation of the $\overline{PSI}$ value for the substrate inverse pole figure presented in Fig. 7b returns the value of 0.31. Therefore provided that the inverse pole figure for the specimen substrate is known (calculated from ODF), one can determine the relative pitting susceptibility of that surface using Eq. (7).

**Table 2**
The values of the constants ($A_l$) represented in series of generalized spherical harmonics (Eq. (1)).

| Constant ($A_l$) | $A_2$ | $A_4$ | $A_6$ | $A_8$ | $A_{10}$ |
|---|---|---|---|---|---|
| Value $\times 10^{-3}$ | 0.492 | 2.081 | −4.226 | 3.391 | −1.146 |

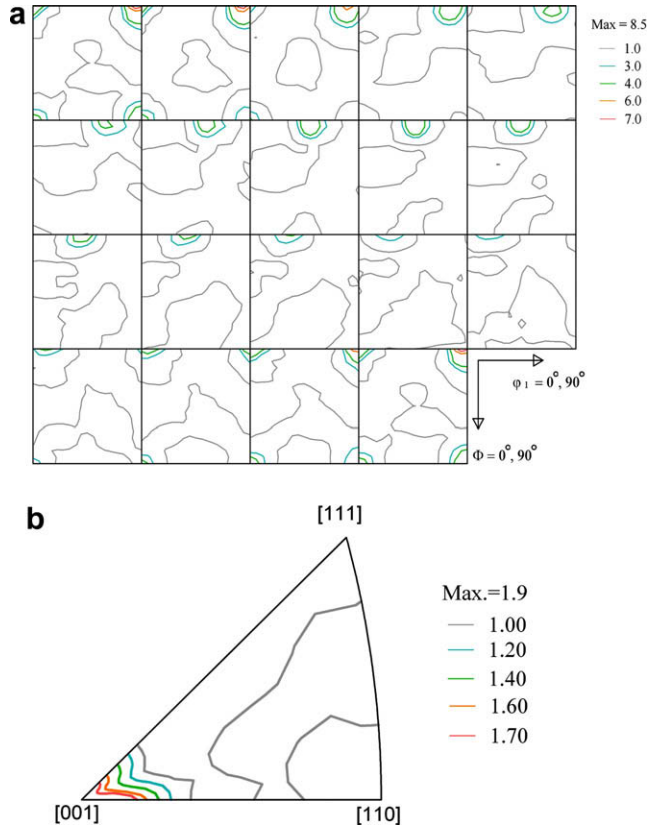


**Fig. 7.** (a) Orientation distribution function (ODF) and (b) Inverse pole figure of SS316LVM substrate showing the texture on a randomly selected area on the surface. The inverse pole figure is calculated in the normal direction of the substrate using TexTool software. The normal inverse pole figure of the substrate clearly shows preferred orientation of {001} planes.

## 4. Conclusion

Results presented in this study prove the anisotropic nature of pitting initiation on the surface and indicate that the pitting corrosion susceptibility of the grains is dependent on the crystallographic planes. It has been shown that the planar orientation, {111} and {100} have the highest resistance to pitting corrosion and generally a lower pitting resistance is expected for the crystallographic planes with lower atomic density. The generalized spherical harmonic functions were used to describe the pitting initiation susceptibility of various crystallographic planes. Using the proposed description and the texture inverse pole figure that characterizes the frequency of different crystallographic planes on the surface of the investigated material it is possible to predict pitting resistance based on texture measurements. The results obtained demonstrate that texture optimization can become a novel tool for improving pitting resistance of the SS316LVM.

## Acknowledgements

The authors would like to acknowledge the Natural Science and Engineering Research Council of Canada and the McGill Centre for Biorecognition and Biosensors for support of this research.

## References

[1] D.R. Whittaker, M.F. Fillinger, Vasc. Endovas. Surg. 40 (2006) 85.
[2] J.J. Jacobs, J.L. Gilbert, R.M. Urban, J. Bone Joint Surg. 80 (1998) 268.
[3] M.P. Ryan, D.E. Williams, R.J. Chater, B.M. Hutton, D.S. McPhail, Nature 415 (2002) 770.
[4] P. Schmuki, H. Hildebrand, A. Friedrich, S. Virtanen, Corr. Sci. 47 (2005) 1239.
[5] J. Pan, C. Karlen, C. Ulfvin, J. Electrochem. Soc. 147 (2000) 1021.
[6] M.G. Shettlemore, K.J. Bundy, J. Biomed. Mater. Res. 45 (1999) 395.
[7] Y. Okazaki, E. Gotoh, Biomaterials 26 (2005) 11.
[8] G.T. Burstein, R.M. Souto, J. Electrochem. Soc. 151 (2004) B537.
[9] M.A. Barbosa, Corr. Sci. 23 (1983) 1293.
[10] G.S. Frankel, J. Electrochem. Soc. 145 (1998) 2186.
[11] A. Shahryari, S. Omanovic, Electrochem. Comm. 9 (2007) 76.
[12] H.E. Hanninen, Int. Mater. Rev. 3 (1979) 85.
[13] J.M. Bastidas, C.L. Torres, E. Cano, J.L. Polo, Corr. Sci. 44 (2002) 625.

[14] S. Maximovitch, G. Barral, F.L. Cras, F. Claudet, Corr. Sci. 37 (1995) 271.
[15] A. Shahryari, S. Omanovic, J.A. Szpunar, Mater. Sci. Eng. C 28 (2008) 94.
[16] L. Tan, M.T. Machut, K. Sridharan, T.R. Allen, J. Nucl. Mater. 371 (2007) 161.
[17] B.R. Kumar, R. Singh, B. Mahato, P.K. De, N.R. Bandyopadhyay, D.K. Bhattacharya, Mater. Character. 54 (2005) 141.
[18] H. Park, J.A. Szpunar, Corr. Sci. 40 (1998) 525.
[19] S.V. Phadnis, A.K. Satpati, K.P. Muthe, J.C. Vyas, R.I. Sundaresan, Corr. Sci. 45 (2003) 2467.
[20] H.F.G. Abreu, S.S. Carvalho, P.L. Neto, R.P.d. Santos, V.N. Freire, P.M.O. Silva, S.S.M. Tavares, Mater. Res. 10 (2007) 359.
[21] A. Barbucci, M. Delucchi, M. Panizza, M. Sacco, G. Cerisola, J. Alloys Compd. 317–318 (2001) 607.
[22] B. Maza, P. Pedeferri, D. Sinigaglia, A. Cigada, G.A. Mondora, G. Re, J. Electrochem. Soc. 126 (1979) 2075.
[23] M. Drogowska, L. Brossard, H. Menard, J. Appl. Electrochem. 28 (1998) 491.
[24] T. Suter, H. Bohni, Electrochim. Acta 42 (1997) 3275.
[25] J. Kruger, J. Electrochem. Soc. 106 (1959) 736.
[26] S.Y. Park, J.H. Kim, M.H. Lee, Y.H. Jeong, J. Nucl. Mater. 376 (2008) 98.
[27] B.W. Davis, P.J. Moran, P.M. Natishan, Corr. Sci. 42 (2000) 2187.
[28] M. Yasuda, F. Weinberg, D. Tromans, J. Electrochem. Soc. 137 (1990).
[29] H.-J. Bunge, Texture Analysis in Materials Science-Mathematical Methods, Butterworth-Heinemann, Oxford, 1983.